CHAPTER 6

Hysteretic Finite Element Model Updating

Analyzing the seismic responses measured on the Parkfield school building using MODE-ID and hysteresis curves has provided several important insights into the characteristics of wood-frame structures. However, to accurately simulate the nonlinear behavior of the structure, a more extensive analysis is needed. The finite element method is a powerful numerical analysis that has been widely applied in various engineering fields. This chapter presents the finite element procedure and models used to characterize the Parkfield school building. Model updating procedures will be applied based on recorded response and various updating routines.

Creating representative models serve several purposes. First, it serves as a validation tool to assess the hysteretic extraction process as mentioned in Chapter 5. Second, the model can simulate and predict responses from various earthquakes. This can decrease the number of expensive experimental tests that need to be conducted. Furthermore, the predicted responses can be used to update building codes. Lastly, the development of accurate models will attest to the value of the instrumentation program. A

database of seismic records that is continually updated serves as a perfect complement to the updating of models.

The challenge in creating these models from data is that this inverse problem is ill-conditioned because not all data records provide information on the nonlinear behavior. Furthermore, the process is complicated by the number of parameters needed to characterize the hysteretic restoring force of the building. Without sufficient data, tradeoffs are seen among the parameters, making the system unidentifiable. This chapter will discuss the different model updating techniques used to find an appropriate model. The chosen model will simulate the Parkfield records and provide information in the physical behavior of the structure during the earthquake.

6.1 Finite Element Procedure

A simple mathematical model of a wood-frame building during an earthquake response uses plane stress elements for the walls and diaphragm. The finite element program was written specifically to model tilt-up buildings. A modified version was used to model wood-frame structures.

In this model, a node can contain six degrees of freedom: translations u_i, v_i and w_i in the global X, Y and Z directions and rotations θ_i, γ_i, and α_i about these axes, where i denotes node i. Element matrices and vectors are first created in a local coordinate system x', y', z'. They are then rotated to the global reference frame for assembly.
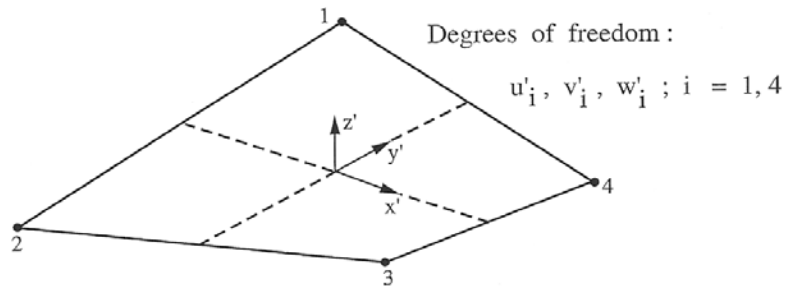
Figure 6.1: Geometry of the plane stress element.

6.1.1 Elements

Plane stress elements are standard 4-node quadrilaterals whose local coordinate system in shown Figure 6.1. Evaluation of the elements is done through 2-by-2 Gauss integration. For linear behavior in the element, the stresses and strains are related in the conventional way by defining Young's modulus, Poisson's ratio and shear modulus. For nonlinear behavior, the relation between the shear force and shear strain are dictated by the hysteretic behavior shown in Figure 6.2. No stiffness degradation is implemented at the moment. When nonlinearity is present for shear, the linear relation is still used for the normal stresses and strains. Material parameters can be specified either for the actual thickness or a unit thickness. The program uses a constant average acceleration time integration scheme to solve the matrix equation of motion. The tangent stiffness matrix and diagonal mass matrix are assembled from each of the individual elements, while the damping matrix is constructed through Rayleigh damping.

The main reason for choosing plane stress elements is the fewer number of parameters used to compare to a plate element. Although some of the moment and bending

parameters can be inferred from a detailed structural plan, the aim here is to develop

models directly from the amount of information provided online. Highly detailed models

through a study of structural plans can be useful, but the current instrumentation would not

be able to fully support this procedure. Another reason for choosing plane stress elements is

that the expected response from a one-story building would predominantly be shearing

motions as opposed to bending motions.
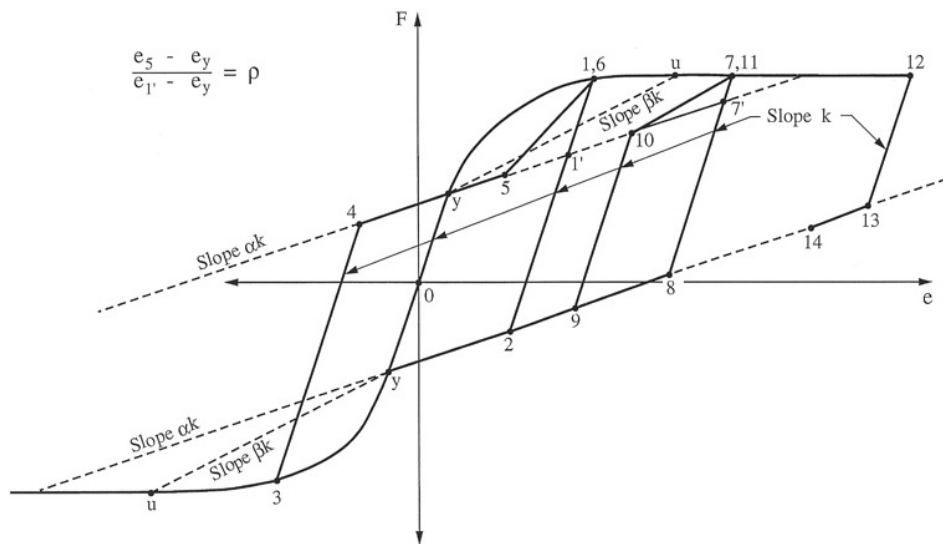
Figure 6.2: Hysteresis behavior with pinching. F is a generalized action and e is a generalized deflection. Required parameters are F_y, F_u, k, α, β, and ρ where y = yield and u = ultimate. An illustrative history follows the path 0-1-2-3-4-5-6-7-8-10-11-12-13-14.

6.1.2 Models

The numerical modeling procedure uses the results from MODE-ID as a basis. The ratio of the mass and stiffness of the elements are adjusted accordingly so that the fundamental frequencies of the Parkfield school building model match the fundamental modes identified through MODE-ID. Acceleration records from the numerical model and recorded data from the building will be compared at corresponding locations. It is important that the relative acceleration is used for comparison, as the total acceleration is largely dominated by the ground motion. The extracted hysteresis curves are also useful in correcting the model. As shown previously, the extraction method should provide insights into the hysteretic behaviors that the model needs to mimic. Therefore, attempts to model the relative acceleration are also largely dependent on implementing similar hysteretic characteristics.

A variety of finite-element models were considered in the process. Figure 6.3 shows the different types of discretizations used. All the ground nodes are constrained in all six degrees of freedom while the roof nodes can move in the transverse and longitudinal directions. Depending on the nonlinearity and the model resolution, each simulation can take 30 seconds to a minute.

The model on the left in Figure 6.3 consists of 42 nodes and 29 elements. Each roof element is 10' × 8', the north and south wall element are 8' × 12', and the east and west wall element are 10' × 12'. This discretization does not take advantage of the acceleration time history on top of the south shear wall since the height of the model is one element. The middle model in Figure 6.3 provides multiple elements along the height of the model.

78 nodes and 58 elements were used. Each of these models served as a basis for deriving

models with openings shown in Figure 6.4.
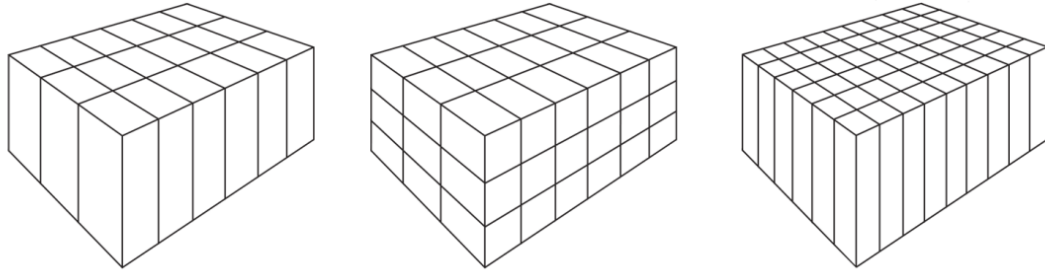
Figure 6.3: Sample of the different types of model discretizations used (south-west point of view).
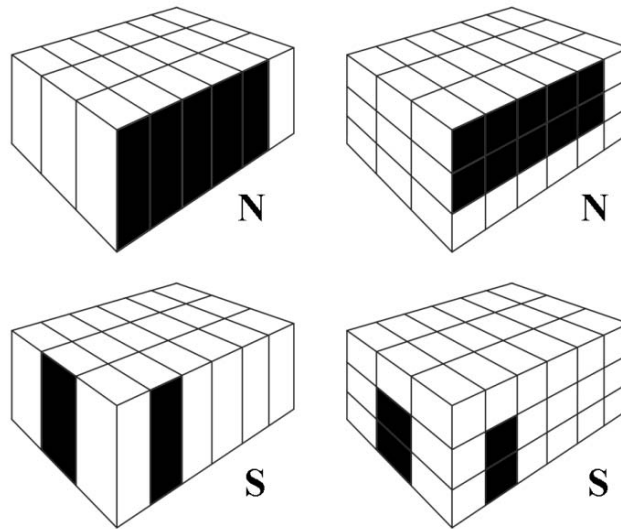
Figure 6.4: Black elements show the windows and door openings in the structure. The procedure models these as openings.

Based on physical intuition, including these openings should improve the data fit of the model. However, results showed poor data fit and lack of convergence. It is possible that in this finite element model framework, better fit can be achieved by not modeling these openings. Furthermore, complications occur with the use of plane stress elements along the height discretization of the building. Additional constraints are needed at these nodes to keep the problem numerically stable. The restraints are not representative of the building's behavior.

Instead of incorporating the openings, each face of the building is modeled as one equivalent wall. The model on the right in Figure 6.3 consists of 80 nodes and 66 elements. Each roof element is 6' × 6' and each wall element is 6' × 12'. This discretization does not take advantage of the acceleration time history on top of the south shear wall since the height of the model is one element. Figure 6.5 shows the 80-node model with three different configurations. The different shades of gray indicate a different set of parameters is used to characterize the structural component. A list of parameters in each set is shown in Table 6-1.
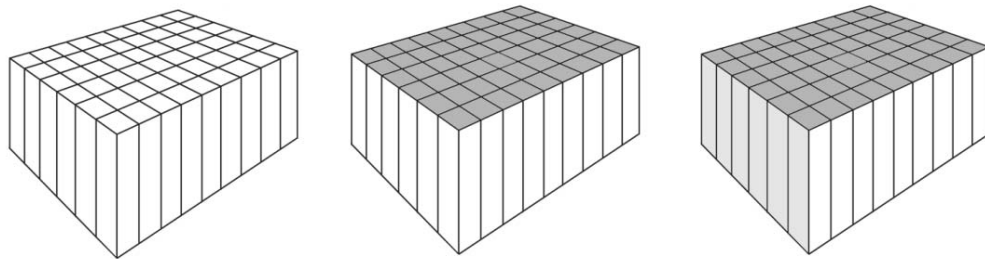
Figure 6.5: (From left to right) Model 1. Walls and diaphragm have same set of parameters. Model 2. Walls and diaphragm have different set of parameters. Model 3. East-West walls, North-South walls, and diaphragm have different set of parameters.

114

Table 6-1: List of parameters used to characterize a structural component.

Parameter	Description	Parameter	Description
POI	Poisson's Ratio	**GG**	Shear Modulus
BET	Hysteretic Parameter: Slope 1	**ALP**	Hysteretic Parameter: Slope 2
RP	Hysteretic Parameter: Return Path	**SXY1**	Shear Yielding Strength
SXYU	Shear Ultimate Strength	**K**	Young's Modulus
DAMP	Rayleigh Damping (one value per model)		

Aside from geometric information and the parameters listed above, other variable inputs include the mass and thickness of the elements. These values are kept constant to help narrow the inverse problem. When the Parkfield earthquake is added as ground motions, the model performs a dynamic analysis to calculate the acceleration and displacement time histories.

6.2 Validating the Hysteretic Extraction Process

Prior to searching optimal parameters for the model, an index wood-frame structure having the same dimensions as the Parkfield school building was assembled in the finite element program. The purpose is to provide insights into the effects of ground motion perpendicular to the sensors. As described in Chapter 5, the hysteresis extraction process worked well for the uni-axial shake table tests, but the results for field records were less conclusive. This validation process simply involves different ground motion inputs, the number of

acceleration channels used, the presence of viscous damping forces, and the degree of nonlinearity in the elements. The following hysteresis curves in Figures 6.6 and 6.7 represent the behavior on the east wall of the building.

Figure 6.6 presents a scenario where a structure behaves linearly under earthquake loading. The calculated and extracted hysteresis curves are expected to be straight lines without viscous damping. However, in Figure 6.6a, even without the presence of the East-West horizontal ground motion, some discrepancies may be seen. The sway in the middle portion of the hysteresis curve comes from the error in the doubly integrated acceleration records. With proper treatment through filtering or removing linear trends in the displacement record, the expected hysteresis curve in Figure 6.6b can be obtained. Figures 6.6c and 6.6d depict the hysteresis curves with the addition of the East-West horizontal ground motion. The only difference is that Figure 6.6d is obtained from the two acceleration records corresponding to Parkfield sensor locations 1 and 2, whereas 6.6c is solely from the acceleration record from location 1. Figures 6e and 6f plot the same curves presented in Figures 6c and 6d but with the addition of viscous damping in the structure. It appears that the extraction process appears to be in good agreement with the calculations of the model despite changing certain factors.
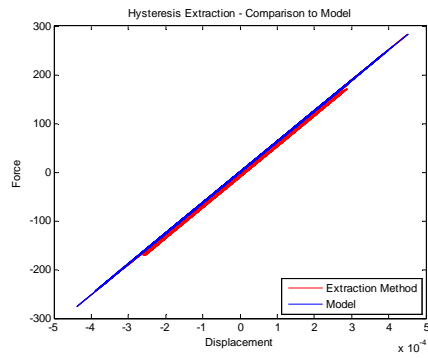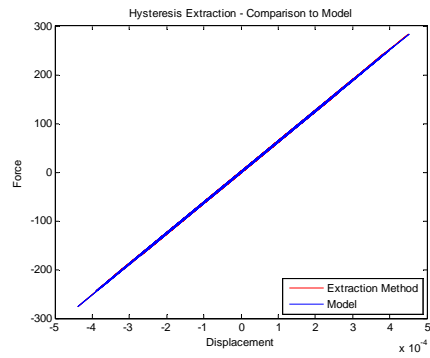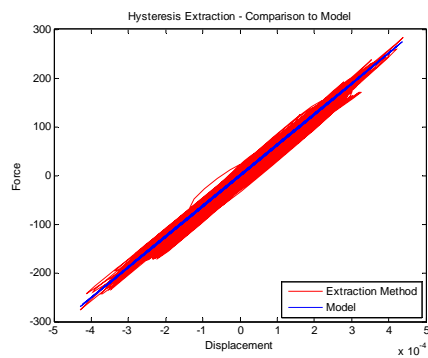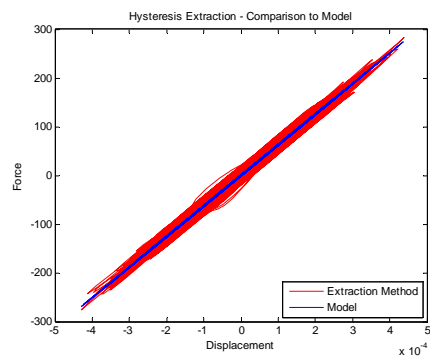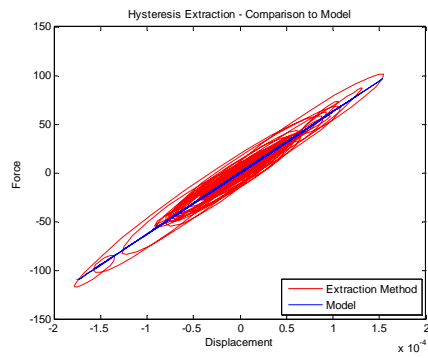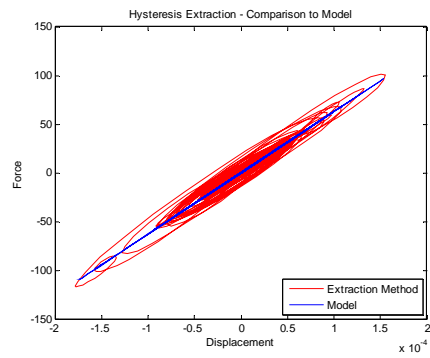
Figure 6.6: Parkfield Earthquake Input – Linear Model a) No horizontal ground motion b) No horizontal ground motion but with adjusted displacement time c) With horizontal ground motion and obtained from an east wall sensor location d) With horizontal ground motion and obtained from Parkfield sensor locations e) Add viscous damping in the model and obtained from an east wall sensor location f) Add viscous damping in the model and obtained from Parkfield sensor locations.

Figure 6.7 presents a different scenario where a structure behaves nonlinearly under earthquake loading. Again, Figure 6.7a demonstrates that, without viscous damping, the extraction method can perfectly retrieve the hysteresis curve from acceleration records. However, with the presence of East-West horizontal ground motion and limitations on the number of sensors, the extraction of the hysteresis curve becomes less accurate, as shown in Figure 6.7.
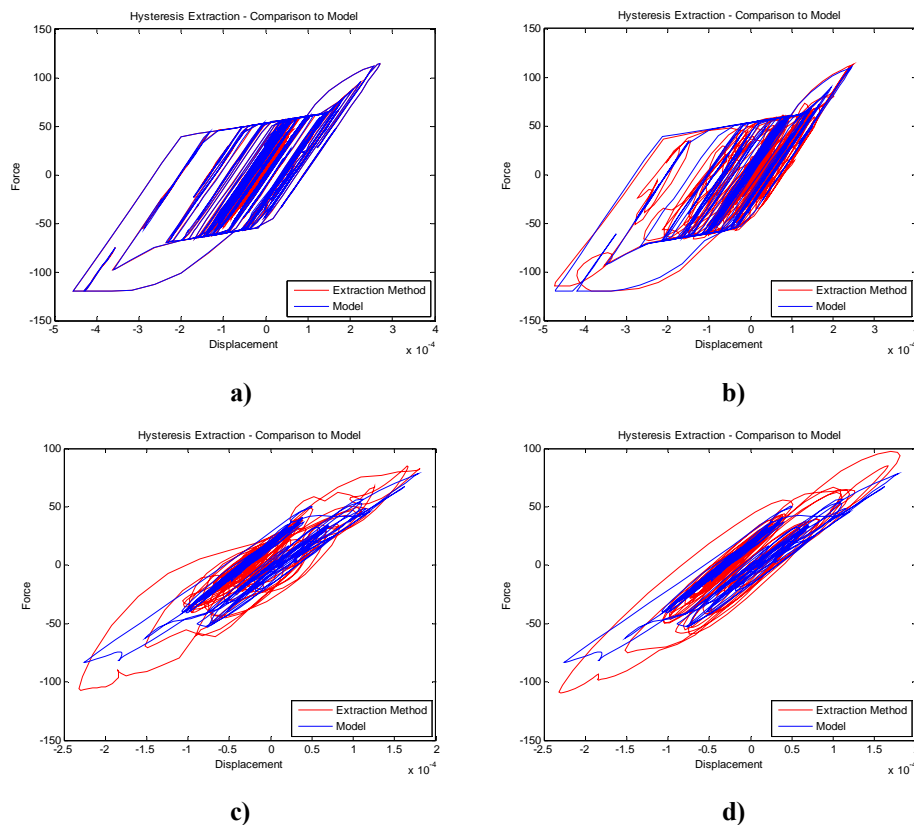
Figure 6.7: Earthquake Ground Motion Input – Nonlinear Model. a) No horizontal ground motion b) With horizontal ground motion c) Add 10% viscous damping in the model and obtained from an east wall sensor location f) Add viscous damping in the model and obtained from Parkfield sensor locations.

This behavior is consistent with the observations in Chapter 5, where hysteretic curves derived from uni-axial ground motions yielded near-perfect extraction, while bidirectional ground motions tampered with the fidelity of the extraction due to the nonlinear forces applied on the walls from the shearing of diaphragm.

By including viscous damping the discrepancies are further magnified, as shown in Figure 6.7c. Figure 6.7d presents the hysteresis curve when Parkfield acceleration records from two sensor locations are used in the FBD approach as described in section 5.2.1. It is clear that simply integrating the acceleration record – which is common practice – on top of the east wall (Figure 6.7c) does not perform as well as the FBD approach (Figure 6.7d). More importantly, this highlights the importance of sensor placement, the types of measurements to be recorded, and the number of sensors needed for each instrumented station.

6.3 Model Optimization

Aside from being a validation tool, the predicted responses from the model can be used for building code design. However, this requires the model to reflect accurately both linear and nonlinear behaviors of the structure. The metric for evaluating the model's fidelity would rely on comparing recorded and simulated seismic responses. In the search for an "optimal" set of parameters, finite element model updating techniques must be used. Finite element model updating is a process of searching for a model that better reflects the measured data than the initial starting model. There are several approaches in implementing least-squares

updating process (Parker 1977; Sambridge 2002; and Tarantola 2005). This section will discuss some routines from both direct and gradient search methods.

6.3.1 Direct Search Methods

Direct search methods are a class of techniques that do not involve finding extrema of the objective function with calculating derivatives. Instead, results generated from several thousand samples are collectively used to determine a better model. Advanced direct search methods include simulated annealing, which is based on mimicking a natural thermodynamic optimization process that occurs in cooling of a crystal and genetic algorithms that follow a biological analogy that occurs in natural selection. At the most rudimentary level of direct search methods is the uniform search. Uniform search discretizes the parameter space into grids of pre-determined sample points. Each point is simulated and the least-square-error is recorded. Variations of the uniform search include uniform random search, where sample points are not predetermined, and nested uniform search, where the discretization level is finer in areas of lower least-square-error.

The main advantage of uniform search is its ease of implementation. The structure of the routine fits perfectly in parallel computing as none of the simulations depend on any other samples. Uniform search was used as a first measure to understand the data misfit across several combinations of parameters. Each of the uniform searches conducted for the Parkfield school building model involved 3 parameters. The discretization level is 50 samples across each dimension for a total of 125,000 samples for each uniform search. The sample size spanned the range of values that seem probable. The uniform search makes it

easy to analyze the tradeoffs between parameters, as a data misfit surface can be plotted. Figures 6.8 and 6.9 show two of the 150 surfaces that were generated for the Parkfield school building. The model only used one set of parameters.
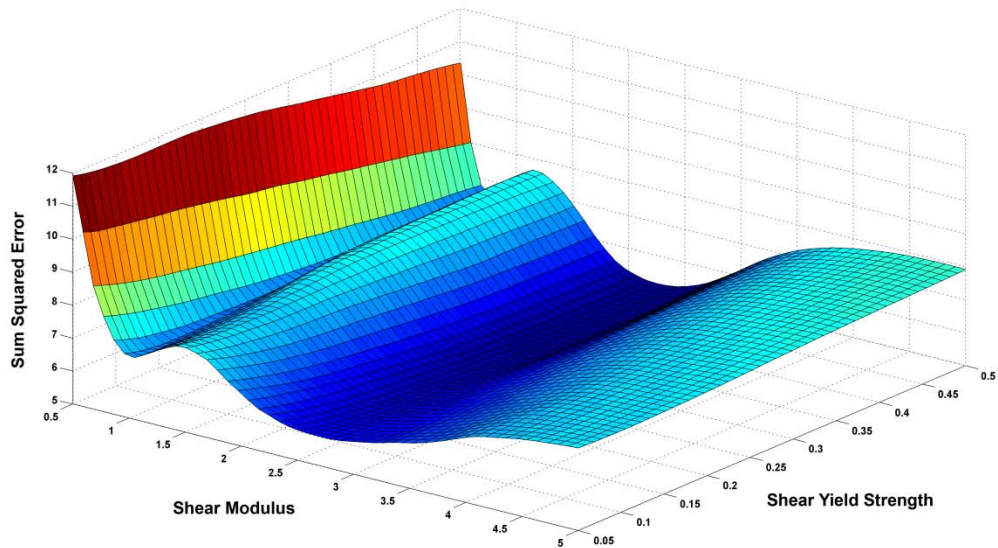
Figure 6.8: Data misfit surface between shear modulus and shear yield strength. Axes values are relative to the nominal values of the parameters.
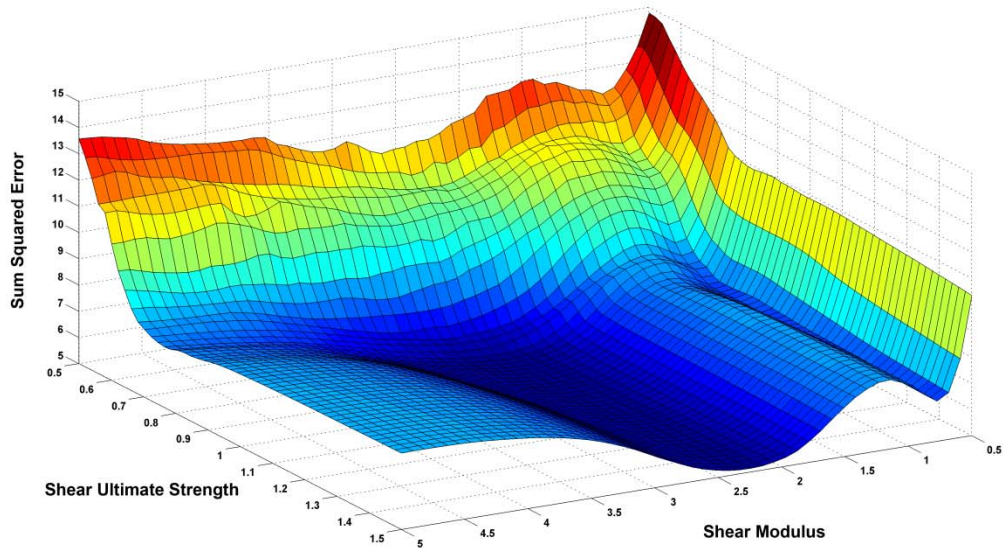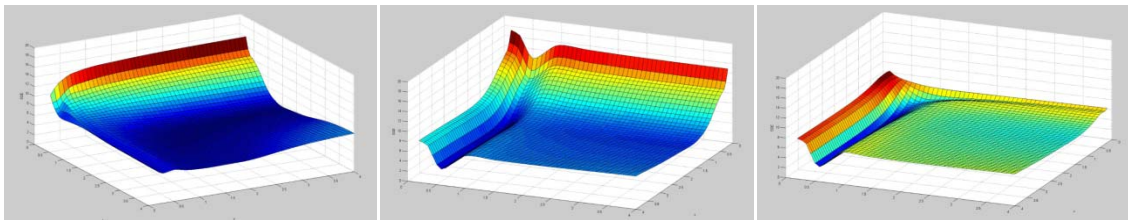
Figure 6.9: Data misfit surface between shear modulus and shear ultimate strength.
Axes values are relative to the nominal values of the parameters.

The data misfit surface in Figure 6.8 shows how the error topology changes with different shear modulus and shear yielding strength. The shear ultimate strength and other parameters are fixed for this surface. The figure shows that the nominal value of the shear modulus performs better than values below it and up to 1.5 times above it. However, at 2.5 times the shear modulus value, a new valley of local minima can be seen. The lowest point appears to be when the shear yielding strength is half its nominal value. The physical interpretation behind this is that the nominal shear modulus may have fit one of the measurements well which matches a particular fundamental mode. However, by increasing the overall shear stiffness of the building, the data fit for all channels have increased and the model matches more than a single fundamental mode. For Figure 6.9, the shear yielding

strength of the structure is unlikely to be less than half of its nominal value. The valley of minima can be seen again where the shear modulus is at 2.5 times its nominal value. The shear ultimate strength does not seem to play a factor in the topology until it is 0.6 times its nominal value. This threshold occurs probably when the numerical model has exceeded its shear ultimate strength. Since the error reported in that region is high, it is unlikely the building surpassed its ultimate strength.

The uniform search was also performed on models with multiple sets of parameters. Figure 6.10 shows the comparison of shear modulus among the east-west walls, north-south walls, and the diaphragm. Without going into full detail, multiple minima and tradeoffs between the parameters are evident. The topologies suggest that the diaphragm shear modulus should be half of its nominal value.

Figure 6.10: Data misfit surfaces of the shear modulus from all three subcomponents of the building.

Although uniform search is easy to implement and data misfit surfaces are simple to understand, the method is inefficient and impractical for problems with high dimensions, as there are issues in choosing discretization levels and number of samples. The method also makes it difficult to present the results in a collective manner. Since the Parkfield school

building model can have up to 26 parameters, the uniform search is only useful in studies on specific parameters.

6.3.2 Gradient Search Methods

Gradient search methods, as the name implies, utilize the gradients of the parameters to determine the minimum of an objective function. The objective function usually takes the form of the data residual term plus some regularization terms (Aster 2004). Gradient methods often incorporate least squares or damped least square solutions in minimizing the objective function. A common feature of the objective function is that not all parameters are constrained by the data. A regularization term is often included in the objective function to provide additional constraints and thus reduce the non-uniqueness of the problem. A main assumption for gradient methods is that the objective function is smooth enough to make use of the derivatives.

Instead of pre-selecting all simulation points in a uniform search, gradient methods use iterative steps and select a new simulation point for each successive approximation to the solution. This approach eliminates unnecessary simulations that do not contribute directly to the optimization of the problem. However, calculations for the gradient vector can become costly as well. For example, the finite central difference method would require performing twice the number of parameters of simulations at the initial guess to estimate the gradient vector. The computational efficiency diminishes if several iterations are needed for optimization.

The simultaneous perturbation stochastic approximation (SPSA) optimization algorithm overcomes the computational hurdle by only requiring two simulations to estimate the gradient vector. This improvement relies on generating the two simulation points from random perturbations of all the parameters of the initial guess. The optimization algorithm follows a recursive equation (Equation 6-1), starting with an initial guess $\boldsymbol{\theta}_0$:

$$\boldsymbol{\theta}_{k+1} = \boldsymbol{\theta}_k - a_k g_k(\boldsymbol{\theta}_k) \tag{6-1}$$

$$g_k(\boldsymbol{\theta}_k) = \frac{V(\boldsymbol{\theta}_k + c_k \Delta_k) - V(\boldsymbol{\theta}_k - c_k \Delta_k)}{2 c_k D_k} \tag{6-2}$$

V : Numerical model

$g_k(\boldsymbol{\theta}_k)$: Estimate of the gradient of V evaluated at $\boldsymbol{\theta}_k$

Δ_k: Perturbation vector $[\Delta_{k1}, \Delta_{k2}, \dots, \Delta_{kD}]$

D: Perturbation distribution (symmetric Bernoulli distribution $P(D_i = 1) = P(D_i = -1) = 0.5$, for $i = 1,2,\dots,D$) (Spall 1998).

$a_k = \frac{a}{(A+k+1)^\alpha}$: Gain sequences with A and α as user selected coefficients

$c_k = \frac{c}{(k+1)^\gamma}$: Gain sequences with c and γ as user selected coefficients

The optimization algorithm requires the parameters to be normalized for numerical stability purposes. Further information regarding the SPSA can be found in Spall (1998) and Cheung and Beck (2008).

The SPSA algorithm was implemented in the optimization of all numerical models. Conclusions regarding inadequate modeling of openings stem from the lack of convergence seen in the SPSA routine. Each SPSA search had a minimum of 500 iterations and stopped when a convergence criteria was met. Each configuration was repeated at least 48 times to incorporate both the same and different initial guesses. A configuration involves selecting

125

the gain sequences, the number of measurement channels for data fit, and the number of parameters to be perturbed. It was necessary to confine some of these factors to obtain a better initial guess.

Results from SPSA demonstrated the lack of convergence to a single set of parameters. This is expected as the nature of system identification hysteretic structures is ill-conditioned. It is inevitable that there will be tradeoffs between the parameters that can produce similar results. The parameter set that yielded the least data fit error was chosen from the SPSA result. The predicted responses are shown in Figure 6.10. The overall data fit is satisfactory, with slightly more discrepancies in channel 1. However, the hysteresis curves obtained from the fit (Figure 6.11) showed behaviors that are not physically representative of wood-frame buildings. Therefore, even with the lowest data fit error, the presented model may not be non-characteristic of real structures.
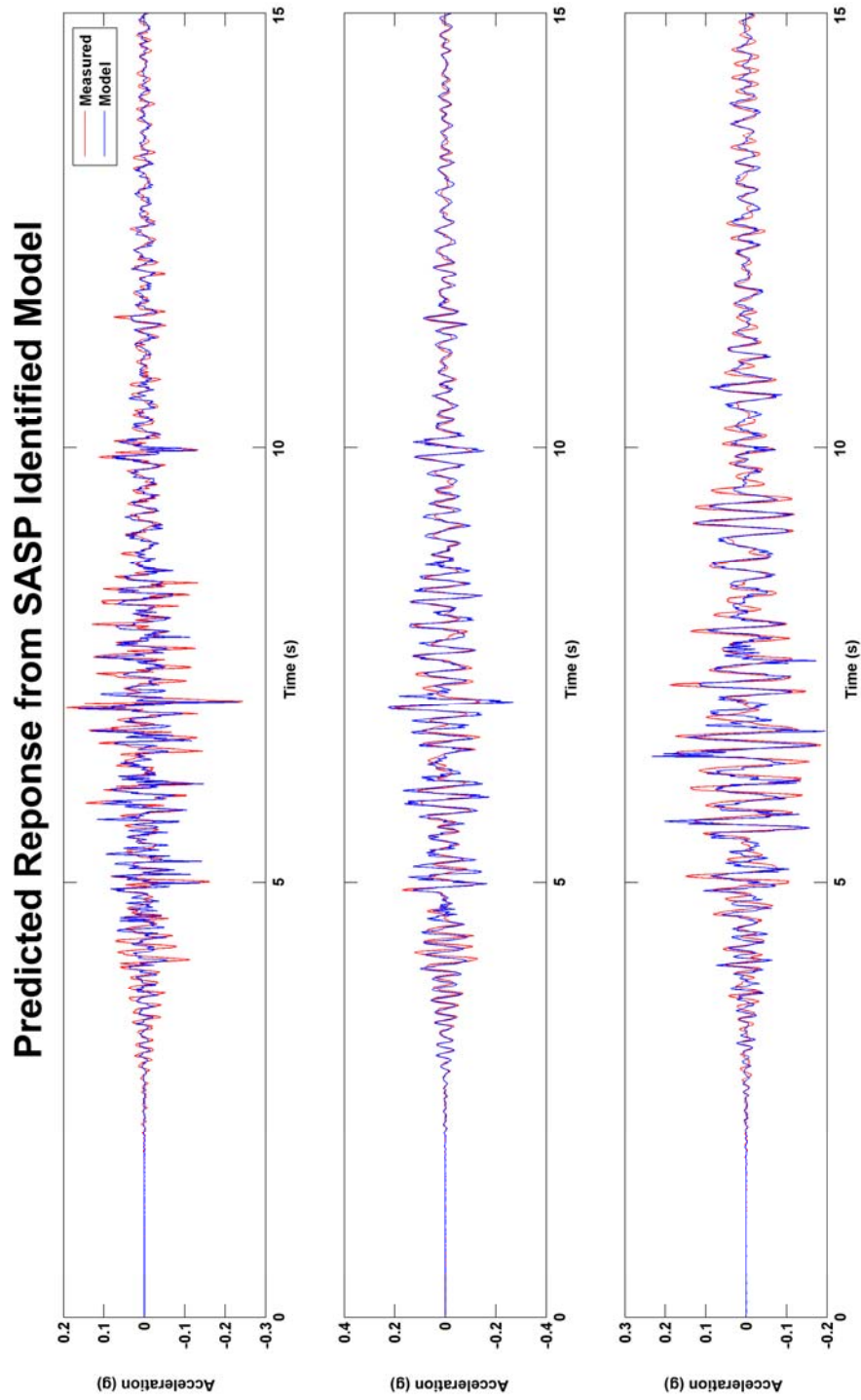
Figure 6.10: Data fit of the Parkfield school record from SPSA identified parameters.
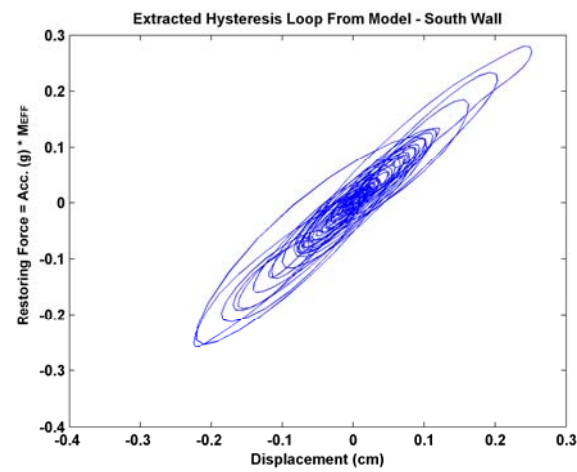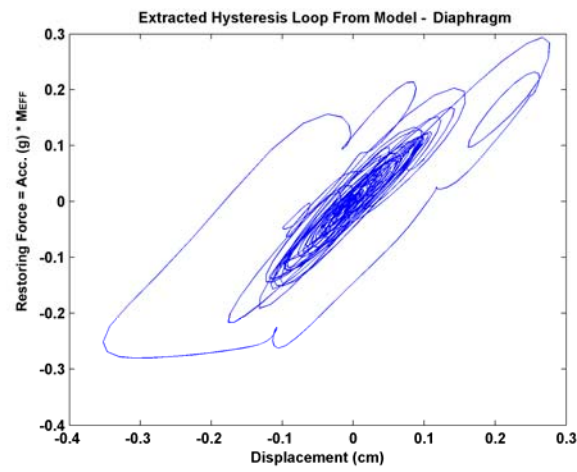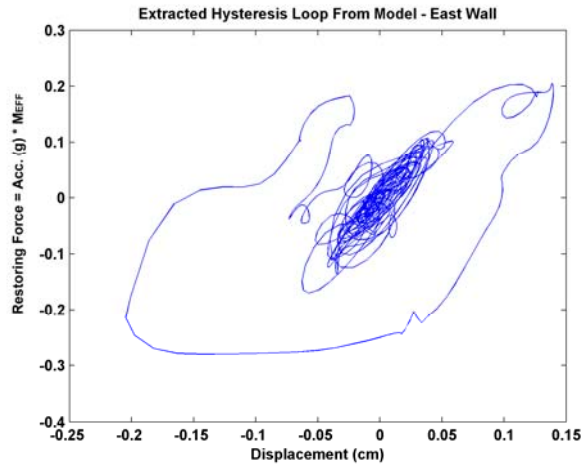
127

Figure 6.11: Hysteresis curves obtained from the SPSA identified numerical model.

128

The SPSA and other gradient methods have the advantage of relating the minimization problem to an inversion problem. However, it is necessary to regularize the problem to reduce the non-uniqueness of the problem. In a nonlinear problem that solves for the hysteretic behavior of wood-frame structures, the models are almost always unidentifiable based on the available data. Regularizing a problem will lead to a tradeoff between data fit and model resolution. Also, formulating an initial guess for a gradient method is very important as a problem can converge to one of several local minima as it attempts to find the global minimum. This can be seen when the SPSA algorithm converges to multiple final parameter values during different runs. Since the SPSA routine only provides one solution even though multiple solutions occur in hysteretic structures, the reliability and consistency is a concern when the models are designed for updating building codes.

6.3.3 Bayesian Updating and Model Selection

The Bayesian updating and model class selection approach (Beck and Yuen 2004, Muto and Beck 2008, Beck and Cheung 2009) is similar to direct search methods in simulating several thousand samples, but its ability to deal with ill-conditioned identification problems merits its own section. Given a set of candidate models for a system, the method calculates the probability of each model given a data set. In this Bayesian approach, the probability of a model should not be interpreted as the frequency of an event given similar conditions, but a value quantifying how plausibly each candidate model is based on the data and prior information (Jaynes 2003; Beck and Cheung 2009). Bayesian updating and model selection

is a process where uncertainties in the model are quantified by a probability density functions (PDF). Even uncertainties of an ill-conditioned identification problem such as identifying hysteretic models of structures can be incorporated (Muto and Beck 2006).

The use of a PDF occurs both at the parameter and model selection stage. Since there are always uncertainties in the parameter values, Bayesian updating analyzes the relative likelihood of each combination of parameter values; one can, for example, present only the most probable one. Similarly, out of a collection of candidate models, Bayesian model selection can be used to check which candidate model class is the most probable. By using Bayes' Theorem which states:

$$Posterior\ PDF\ \alpha\ (prior\ PDF)(likelihood\ function) \tag{6-3}$$

$$p(\theta|D,M)\ \alpha\ p(\theta|M)\ p(D|\theta,M) \tag{6-4}$$

$$p(\theta|D,M)\ \alpha\ p(\theta|M) \prod_{i=1}^{N} p(y_i\mid x_i,\theta,M) \tag{6-5}$$

Posterior PDF:	Uses available information to update prior information about the uncertain parameter values.
Prior PDF:	Contains prior knowledge of the parameter values.
Likelihood function:	Quantifies the probability of the parameter combination to resemble the current data set.
θ:	Set of uncertain parameters.
D:	Set of N data points representing input x_i, output y_i.
M:	Candidate Model.
α:	Denotes "proportional"

The most probable model in a model class can be found by maximizing the posterior PDF for the model class. The uncertainties associated with the most probable parameters depend on the shape of the PDF. Typically, given a larger amount of data, the posterior PDF becomes narrower.

The model class selection takes a step further by utilizing the *evidence* (normalizing constant of the posterior PDF) to quantify the information gain and data fit of the model. Beck and Yuen (2004) and Muto and Beck (2008) provide a detailed discussion on this topic. The calculation of the probability of M_i is based on Bayes' Theorem and proceeds as follows:

$$Posterior\ PDF\ = \frac{(prior\ PDF)(likelihood\ function)}{evidence} \tag{6-6}$$

$$p(\theta_i|D, M_i)\ = \frac{p(\theta_i|M_i)\,p(D|\theta_i, M_i)}{EV_i} \tag{6-7}$$

$$p(M_i|D) = \frac{EV_i}{\sum_i EV_i} \tag{6-8}$$

$$evidence = EV_i = \int (prior\ PDF)(likelihood\ function) \tag{6-9}$$

$$= \int_\theta p(\theta_i|M_i)\,p(D|\theta_i, M_i)\,d\theta_i$$

$$= p(D|M_i)$$

To generate samples which are distributed according to the PDF, stochastic simulation methods are needed when dealing with a large number of uncertain parameters.

The Transitional Markov Chain Monte Carlo (TMCMC) method developed by Ching and Chen (2006) is selected for the Bayesian updating of the Parkfield school numerical models. The TMCMC algorithm for generating posterior samples of the modal parameters is a variation of the multiple-stage model updating procedure proposed by Beck and Au (2000, 2002) which uses the Metropolis-Hastings algorithm at each stage. The difference is the Beck-Au method accomplishes the gradual updating by using an increasing fraction of the data while TMCMC does it by introducing a *tempering* exponent on the likelihood function. This exponent works similarly to that of simulated annealing. TMCMC is implemented in a transformed parameter space as proposed by Cheung and Beck (2008) to enhance the efficiency of simulations by reducing the rejection rate in the Metropolis-Hastings algorithm, that is, reducing the number of repeated samples.

This analysis extends the work done by Muto and Beck (2008) by using real data involving hysteretic models of structures. All three 80-node models were considered as candidate models for the Parkfield records. Each level had 1000 samples simulated for the proposal PDF. Models 1 and 2 required 31 levels for the prior PDF to converge to the posterior PDF. Model 3 needed 49 levels. The parameters chosen for updating are the same as those listed in Table 6-1 with the addition of a variance factor. Figure 6.12 shows the samples from the prior PDF (black) compared to the samples from posterior PDF (green) for Model 1. Figure 6.13 shows posterior samples for different pairs of uncertain parameters. From the shape of the correlation plots, it is evident that the hysteretic model is unidentifiable based on the seismic records.
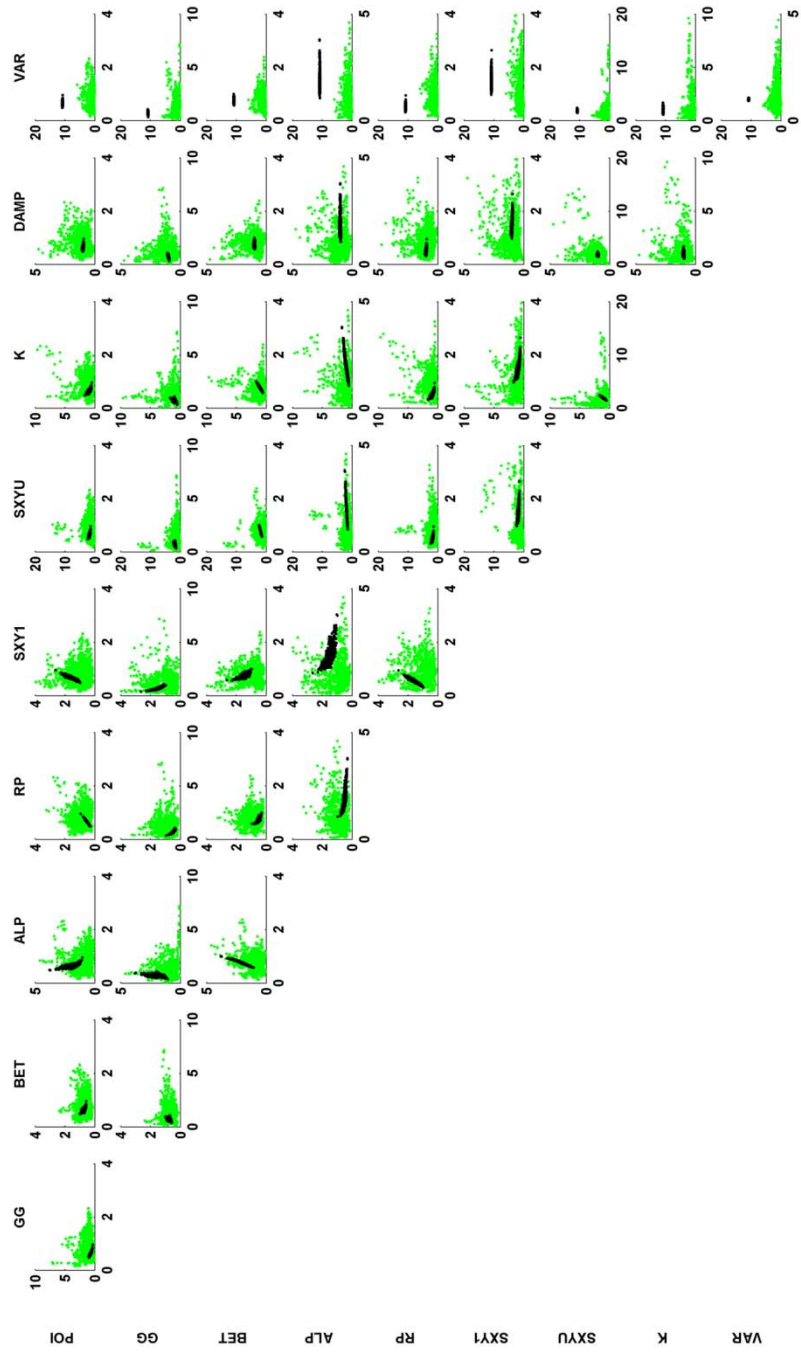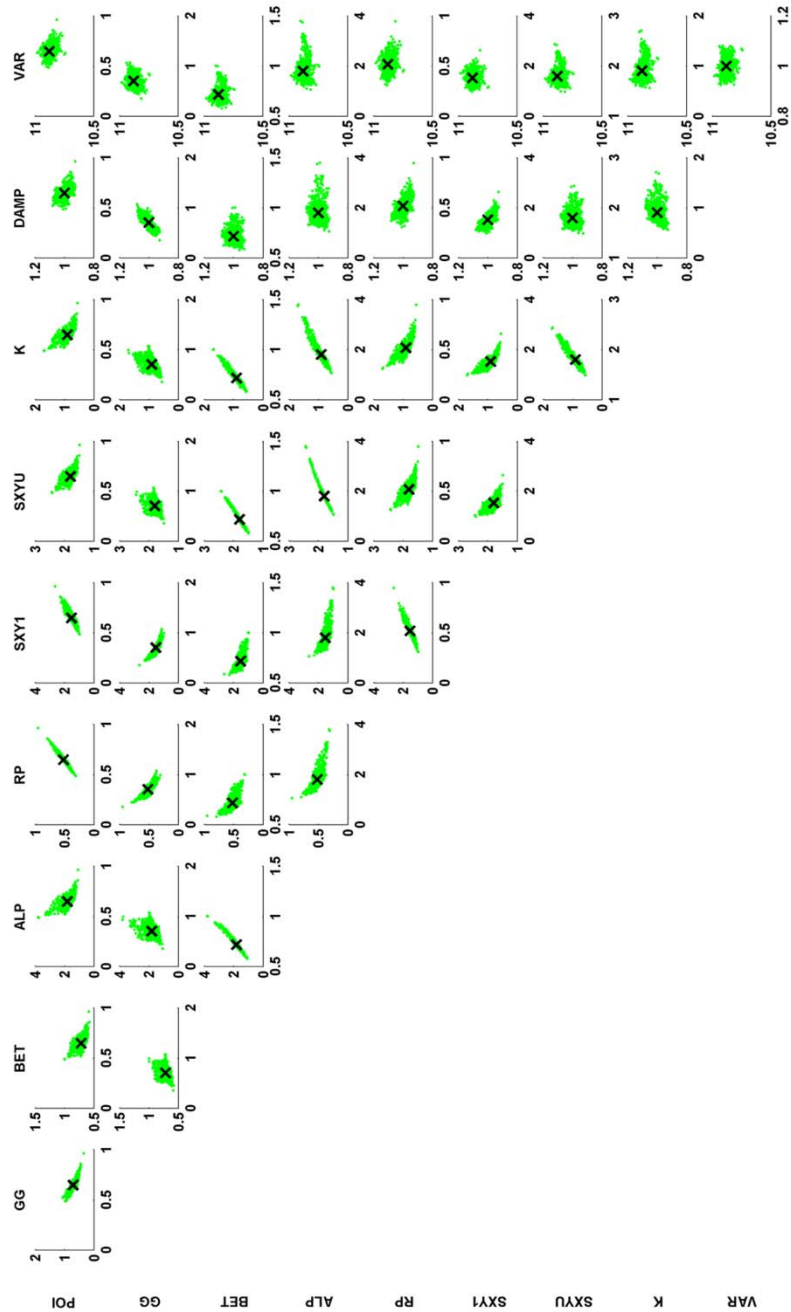
Figure 6.12: Samples from both prior (green) and posterior (black) PDF.

133

Figure 6.13: Posterior samples for different pairs of uncertain parameters in Model 1. X marks the mean of the posterior PDF. This illustrates the difficulty in identifying hysteretic structures.

134

Table 6-2 displays the mean and variance of the parameters in each of the models. The high variance demonstrates the challenges present in identifying hysteretic systems. Future runs can have tighter constraints on the parameters to reduce the variance of the parameters. Model 2 and Model 3 showed significantly lower shear yielding strength than Model 1 at the east and west wall parameters. This suggests that the model potentially uses hysteretic behavior of the plane element for the data fit. Shear yielding strength for the other subcomponents remain relatively higher. Shear moduli across all models and subcomponents have similar values, but reported hysteretic parameters have a very wide range in relation to their nominal values. Another interesting note is that the damping had little fluctuation. The nominal value was 10% and therefore the Bayesian updating suggests a value close to 8% which is consistent with estimates from experimental tests.

Table 6-3 shows the result of the model class selection. Model 3, with a 100% probability, is the most plausible model among the three candidate models, given the Parkfield data. It is not always the case that the most complex model will yield the highest probability since there are penalties involving the value of the "information gain," which describes how much information (in the sense of C. Shannon) is extracted from the data by the model class (Muto and Beck 2008). The higher the information gain from the data, the more the model class is penalized in calculating its posterior probability. However, in this particular case, the larger information gain is countered by the higher value of the data fit. Figures 6.14 show the final data fit from Model 3.

Table 6-2: Mean and standard deviation of the posterior PDF from all candidate models. Note: - indicates values constrained to be same as above parameters.

		Model 1		Model 2		Model 3	
	Parameter	Mean	σ	Mean	σ	Mean	σ
East and West Walls	POI	0.6489	0.0610	0.7017	0.0113	0.2572	0.0075
	GG	0.7078	0.1168	0.6024	0.0170	0.8206	0.0108
	BET	0.7179	0.0644	0.2842	0.0087	0.3358	0.0034
	ALP	1.8088	0.3700	0.3189	0.0103	0.3390	0.0201
	PR	0.5188	0.0792	0.0479	0.0024	0.0882	0.0180
	SXY1	1.5322	0.2338	0.1862	0.0076	0.1802	0.0182
	SXYU	1.8008	0.1381	0.2559	0.0129	0.2258	0.0344
	K	0.9069	0.1726	1.2778	0.0653	1.1914	0.0023
Diaphragm	POI	-	-	0.8205	0.0102	0.5058	0.0076
	GG	-	-	0.9482	0.0333	0.7026	0.0107
	BET	-	-	0.8416	0.0225	0.6840	0.0149
	ALP	-	-	0.0832	0.0036	0.5792	0.0193
	PR	-	-	1.9319	0.0153	0.6142	0.0046
	SXY1	-	-	0.8155	0.0203	0.4471	0.0099
	SXYU	-	-	0.4389	0.0320	3.2640	0.0528
	K	-	-	1.3879	0.0334	2.4600	0.0571
North and South Walls	POI	-	-	-	-	1.2873	0.0158
	GG	-	-	-	-	0.6507	0.0118
	BET	-	-	-	-	0.7644	0.0133
	ALP	-	-	-	-	1.5509	0.0502
	PR	-	-	-	-	0.6242	0.0064
	SXY1	-	-	-	-	1.8261	0.0422
	SXYU	-	-	-	-	1.0314	0.0166
	K	-	-	-	-	1.2139	0.0059
	DAMP	1.0000	0.0321	0.8141	0.0512	0.8445	0.0254
	Var	10.8797	0.0321	10.7768	0.0604	20.64110	0.6545

136

Table 6-3: Bayesian Model Selection with calculated probability of the model.

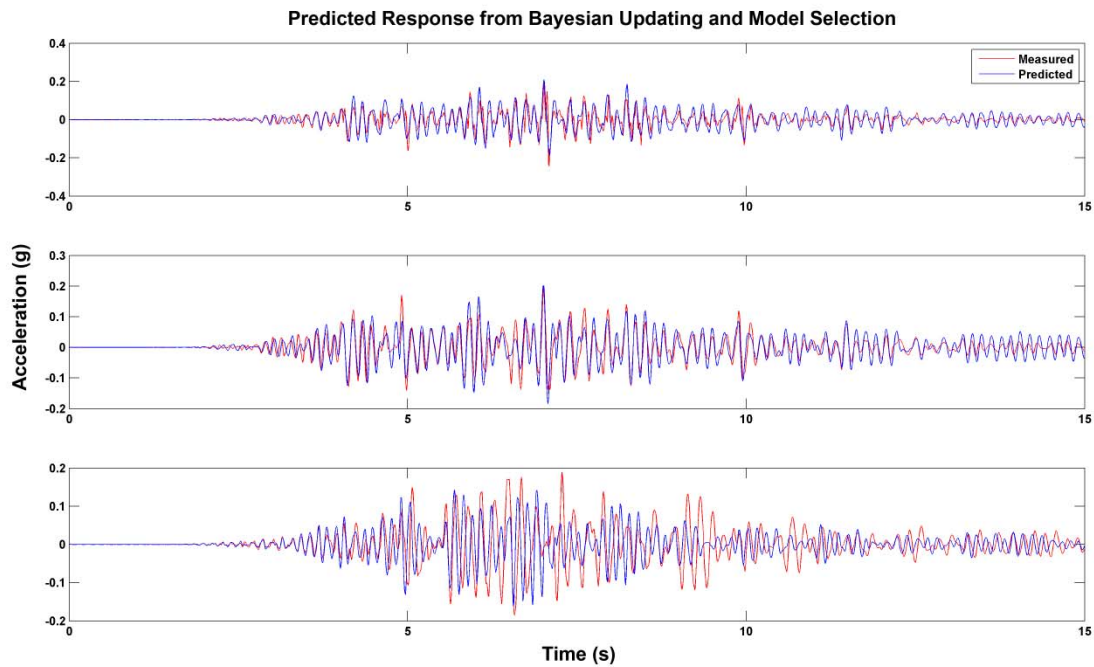|	Data fit (10³)	Information Gain	Log Evidence (10³)	Probability
Model 1	8.70	68.17	8.64	0.0
Model 2	7.93	121.51	7.80	0.0
Model 3	13.49	1000.70	12.48	1.00

Figure 6.14: Data fit of Model 3 predicted by the most probable model from Bayesian updating and model selection.

The Bayesian updating and model selection method was able to provide an appropriate candidate model for the analysis in next section. By dealing with the uncertainties of the model parameters in a probability framework, this method surpasses other routines in

dealing with ill-conditioned problems. Furthermore, the Bayesian framework can be a great method to analyze a strong seismic motion database. The posterior PDFs from past earthquakes can be used to produce prior PDFs for new earthquakes and aftershocks by continual updating of current models. The potential integration is promising in monitoring and enhancing the value of the instrumentation program.

6.4 Model Results

With the use of model updating techniques, sets of model parameters were chosen to simulate the Parkfield response. This section uses the model and parameters selected from the Bayesian framework. Aside from fitting the seismic records, constructing the model provides insights into the physical behavior of the wood-frame structure.

6.4.1 Hysteretic Behavior

The hysteresis extraction process is performed on the acceleration time histories for comparison purposes. In Chapter 5, it was uncertain if the east wall and diaphragm exhibited pinching behavior, while the south wall demonstrated mostly linear behavior. The hysteresis curves from the model are shown in Figures 6.15 through 6.17. Figure 6.15 shows a clear sign of pinching at the east wall, while Figure 6.16 shows a mostly linear response with slight yielding at the extremes. The south wall exhibited a linear response as shown in Figure 6.17. Unlike the hysteresis curves generated from an updated model calculated from the SPSA approach, these hysteresis curves are more consistent with current knowledge of wood-frame structures. The results here also demonstrate why

138

MODE-ID was able to fit the channels at the diaphragm and south wall with a better accuracy compared to the nonlinear behavior seen at the east wall.
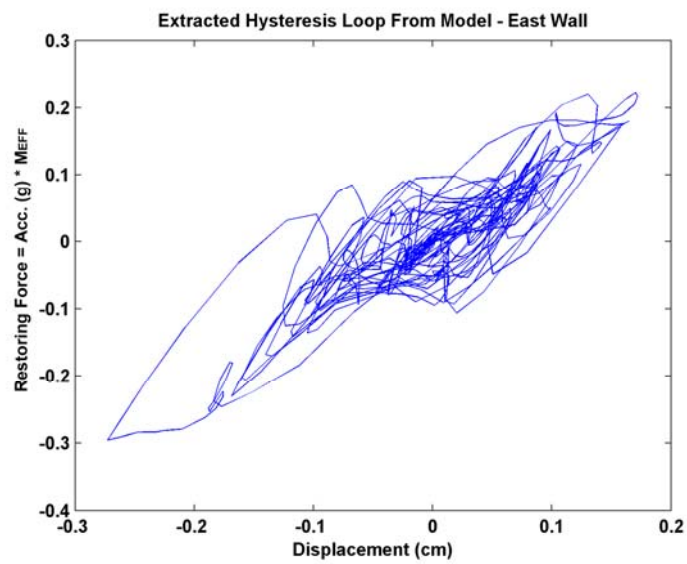
Figure 6.15: Extracted hysteresis loop from east wall. Model chosen by Bayesian model selection.
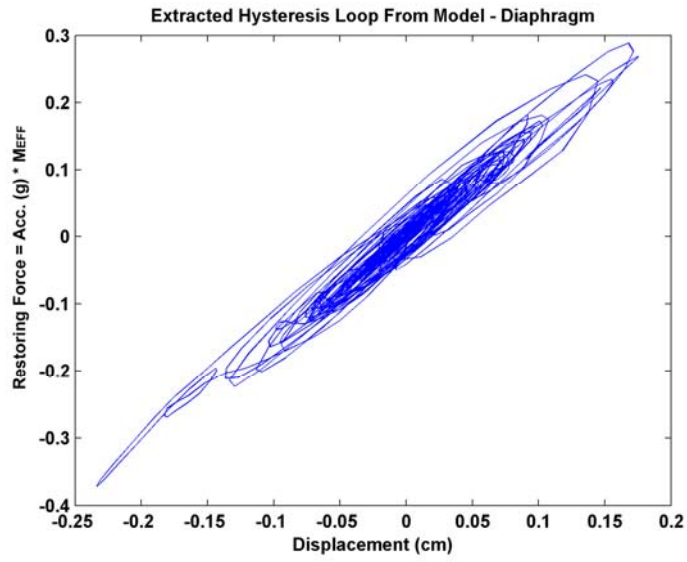
Figure 6.16: Extracted hysteresis loop from diaphragm. Model chosen by Bayesian model selection.
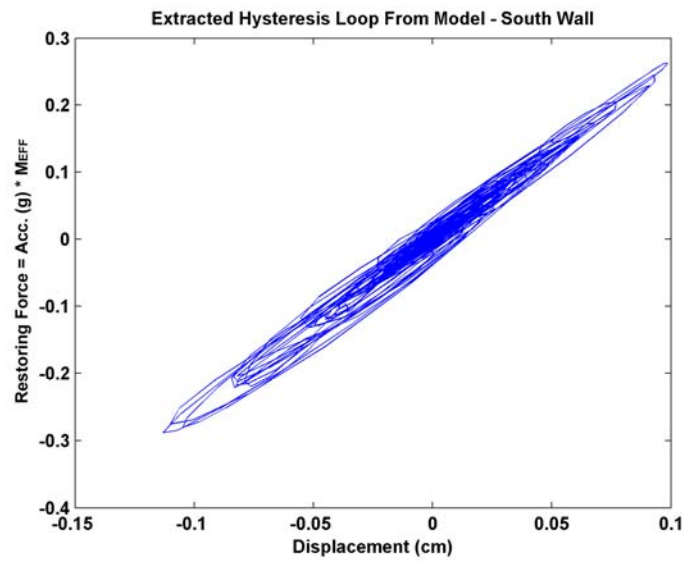

**Figure 6.17: Extracted hysteresis loop from south wall. Model chosen by Bayesian model selection.**

6.4.2 Model Response

The calculated displacement time histories from the model can be used to plot the instantaneous deformations in the wood-frame structure during the Parkfield Earthquake. Figures 6.18 through 6.20 display the progression of the structure's deformation during the seismic motions. Each figure displays a top view of the building with the open circles representing roof nodes. A blue trail for each node marks the relative displacements to the ground at selected time intervals. The displacements are magnified for visual purposes. The largest displacements seen in the figures are at most 0.5 cm.

The diaphragm appears to be flexible and no substantial torsion was observed. The largest deformations can be seen in the plane from the west portion of south wall to the east portion of the north wall. One reason is that the Parkfield Earthquake had strong fault-normal motions toward the northeast and the Parkfield school building was located northeast of the fault. Figure 6.21 displays a close-up version of the displacement particle motions seen in Chapter 3 to demonstrate the strong northeast motion produced from the earthquake. Another reason for the large deformations was the structure's stiffness; in the process of achieving a better fit, the model updating process found that the structure needed to be more flexible. These observations are consistent with the structural drawings in Chapter 3, where a major portion of the right north wall consisted of windows, and the south wall had two doors located near the south-west portion of the wall. These structural openings lower the structural stiffness and allow greater deformations to be exhibited in these local areas.
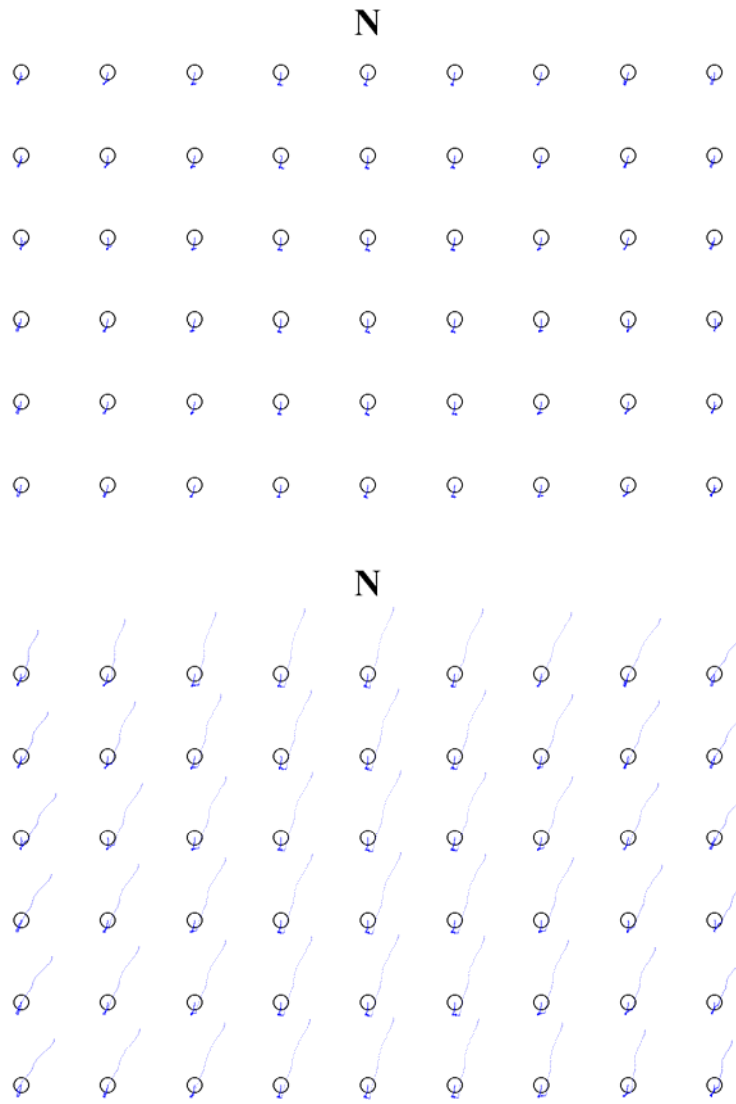
Figure 6.18: (Top) Structural deformations up to the first 2 seconds of seismic record. (Bottom) Structural deformations up to the first 3 seconds of the seismic record.
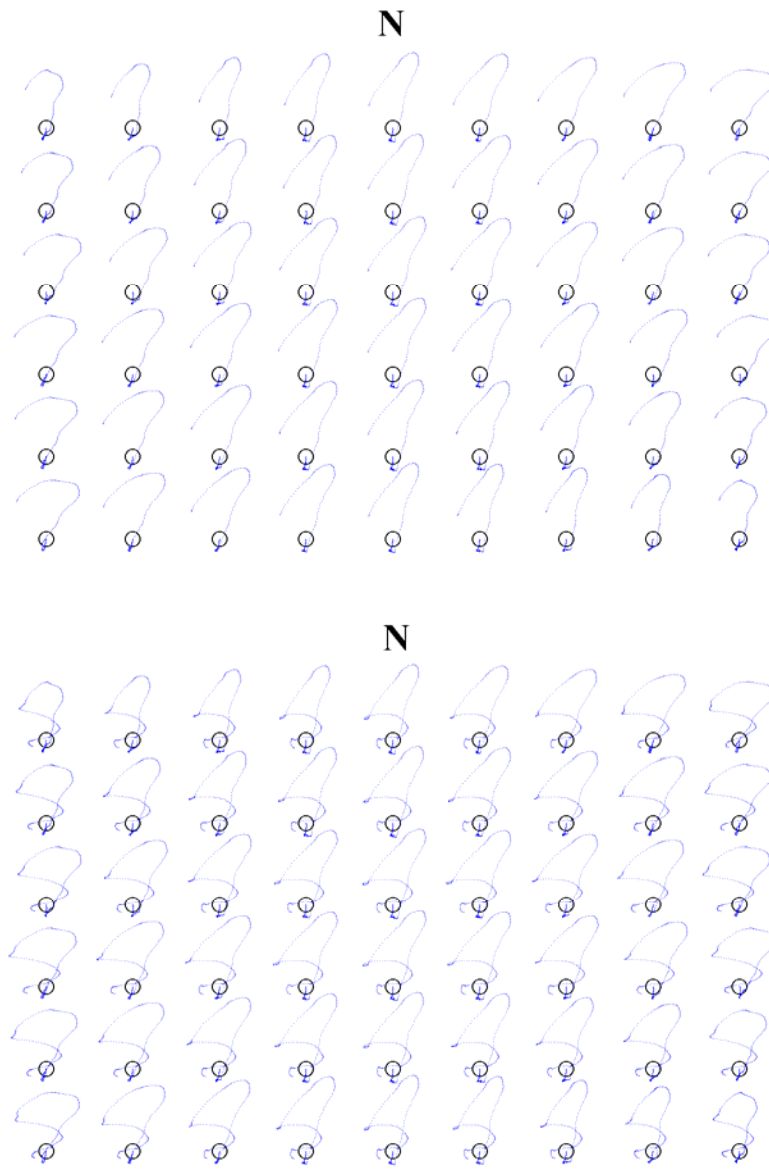
Figure 6.19: (Top) Structural deformations up to the first 5 seconds of seismic record. (Bottom) Structural deformations up to the first 6 seconds of the seismic record.
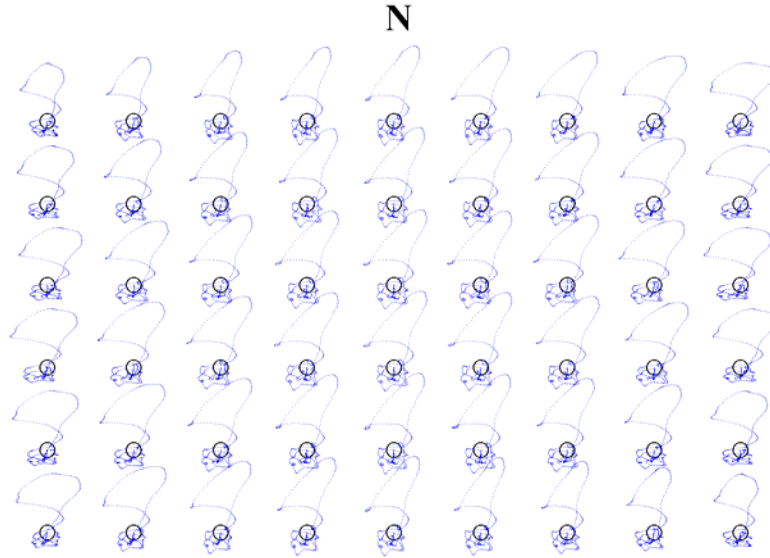
**Figure 6.20: Structural deformations up to the first 8 seconds of the seismic record.**
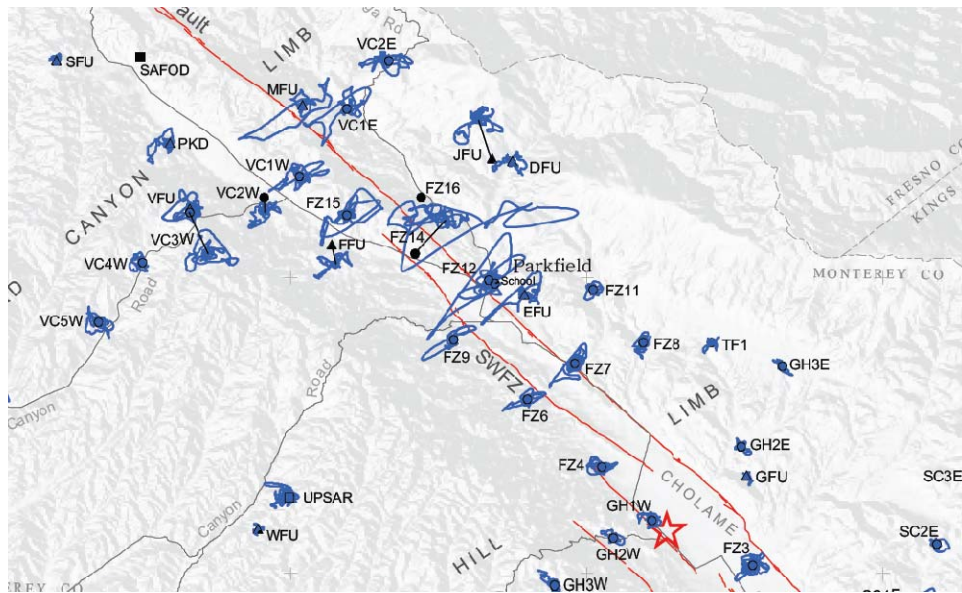
Figure 6.21: Displacement particle motion of instrumented stations during the Parkfield Earthquake. The Parkfield school building is located in the middle of the figure (CSMIP 2006).

144

6.4.3 Energy Dissipation

Model deformations provide an understanding of the structure's behavior during the earthquake, but it is unclear where and how most of the energy dissipation takes place. Using the hysteresis extraction method described in Chapter 5, instantaneous damping estimates can be obtained at various locations of the structure. Figures 6.22 and 6.23 present the energy dissipation of structure based on hysteresis curves. Figure 6.22 analyzes the hysteresis curves obtained from the east-west motion. The shear wall located on the southeast corner of the wall exhibited the highest damping at 10%. Since the model is symmetric, 10% damping can be observed at the northwest corner. However, it is important to note that the northwest corner is much stiffer than the rest of the north wall, which consists mostly of window openings. The rest of the walls and diaphragm exhibited 5% - 8% damping which is expected in a wood-frame structure. Figure 6.23 shows much more energy dissipation with the maximum being more than 20% damping. Most of the dissipation comes from the east and west walls. The flexing motion of the diaphragm in the north-south direction also contributes to the dissipation of energy.

Damping estimates (%) of the building (aerial view) in the East West motion
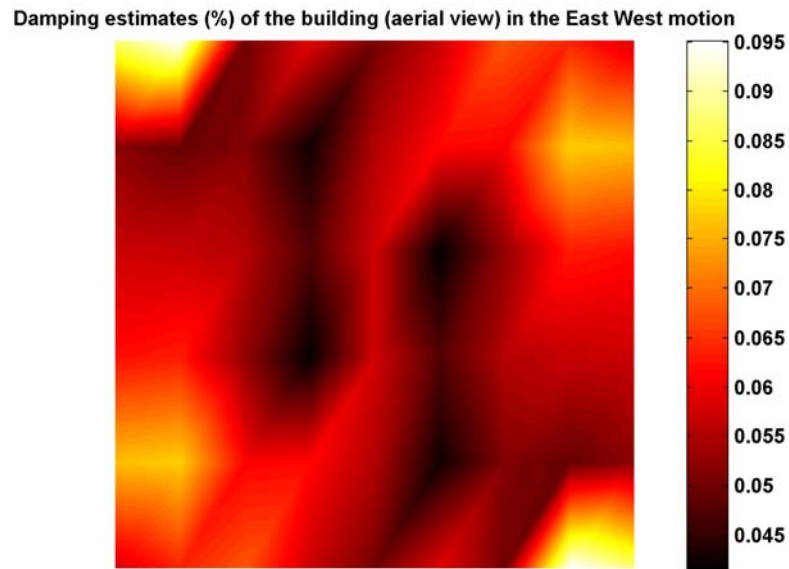
Figure 6.22: Energy dissipation in the east-west motion. 10% damping can be seen at the top left and bottom right corners.

Damping estimates (%) of the building (aerial view) in the North South motion
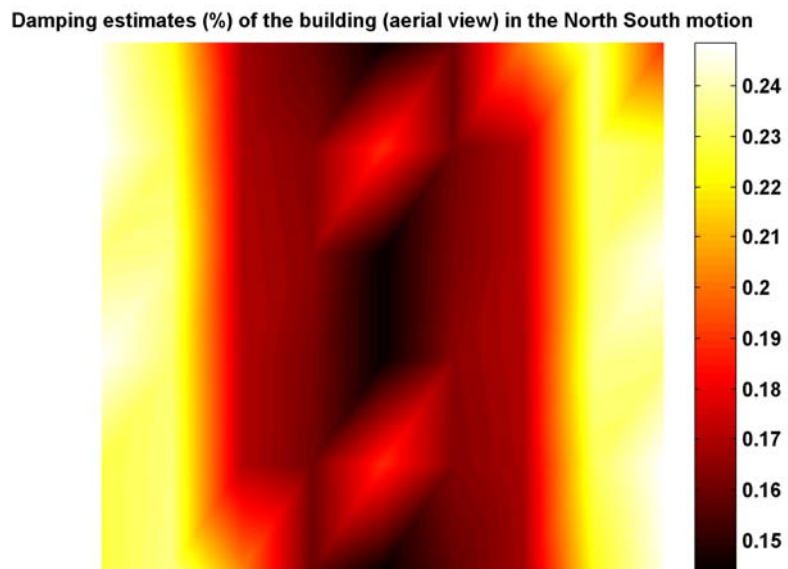
Figure 6.23: Energy dissipation in the north-south motion. More than 20% damping can be seen at east and west walls.

6.5 Conclusions

This chapter presented the finite element modeling and updating procedure and the various models that were considered. The numerical model can be used as a validation tool for the hysteresis extraction process. Paired with finite element model updating routines, the model can also lead to better simulation of seismic records. Different routines were implemented and their advantages and drawbacks were mentioned. Bayesian updating and model class selection stand out for their robustness and quantification of uncertainty. A model can be used to predict based on prior PDFs alone, but using posterior PDFs greatly improves predictions. A Bayesian framework integrated with the CSMIP seismic database can certainly enhance the value of the current instrumentation program by making better use of all earthquake data.

The numerical model achieved a representative data fit and offered insights into the physical behavior of the structure by displaying hysteresis curves and deformation shapes. The model showed signs of pinching hysteresis at the east wall and mostly linear behavior at the other two Parkfield sensor locations. Deformation shapes were consistent with the propagation of the earthquake motion and structural drawings of the building. By using hysteresis curves to calculate damping estimates, the model can also offer insights into the locations of largest energy dissipation.